Regional Studies in Marine Science 103 (2026) 105566

Contents lists available at ScienceDirect

Regional Studies in Marine Science

journal homepage: www.elsevier.com/locate/rsma

Seasonal patterns of surface currents and Lagrangian coherent structures from a decade of high-frequency radar observations in a central California offshore wind energy area

Ryan K. Walter [a,*], Paul Choboter [b], Andres E. Rocha Jayasinha [b,c], Rapha Coutin [b], Corbin Luoma [b], Leah Hoogstra [b,d], Casper Pratt [a,e], Mazen Idriss [a], Emmett Ehrnstein [a], Ian Robbins [a]

[a] Physics Department, California Polytechnic State University, San Luis Obispo, CA, USA
[b] Mathematics Department, California Polytechnic State University, San Luis Obispo, CA, USA
[c] Statistics Department, California Polytechnic State University, San Luis Obispo, CA, USA
[d] Division of Applied Mathematics, Brown University, Providence, RI, USA
[e] Department of Geography, University of California Santa Barbara, Santa Barbara, CA, USA

ARTICLE INFO

Keywords:
Lagrangian coherent structures (LCS)
Finite-time Lyapunov exponents (FTLE)
High-frequency radar (HFR)
Offshore wind energy
California Current System
Marine spatial planning

ABSTRACT

A globally growing Blue Economy, including offshore energy development, requires a baseline understanding of regional oceanographic conditions and current flow fields before installation to be able to evaluate sites and assess impacts on coastal ecosystems. We leverage more than a decade (2012–2022) of high-resolution surface current measurements from a high-frequency radar network along the central California continental shelf, including a previously designated Wind Energy Area (WEA), to characterize seasonal current circulation and identify seasonal patterns in coherent transport structures using a Lagrangian framework. Finite-time Lyapunov exponents (FTLEs) are calculated from surface currents to identify Lagrangian coherent structures (LCS) and characterize seasonal patterns in attracting (convergent) and repelling (divergent) transport structures in the WEA. Mean current patterns exhibited a strong seasonal cycle, with a pronounced transition from relatively weak poleward flow in the winter months to strong equatorward flows during the spring months, before currents relaxed into the late summer and fall. Coincident with the onset of the upwelling season in the spring was a distinct increase in both attracting and repelling FTLE fields, particularly near the coastline, with elevated values extending offshore into the WEA. Attracting ridges exhibited a greater spatial extent and occurrence within the WEA compared to repelling ridges, suggesting a greater propensity for material aggregation (versus dispersal) and prey aggregation (and potential ecological hotspots). These patterns have critical implications for ecosystem dynamics, pollutant transport, and environmental risk in and around the WEA. The analysis presented here could enable the future integration of dynamic oceanographic information, including transport structures derived from the growing international HFR network, into future marine spatial planning, environmental risk assessment, and ecosystem-based management.

1. Introduction

Accelerating climate change and global warming due to human greenhouse gas emissions increasingly threaten ecosystems and economies globally. This has prompted nations worldwide to develop broader renewable energy portfolios that increasingly include offshore wind farms in marine environments (GWEC, 2025). Along the US West Coast, California has ambitious state-mandated goals of 25 GW of offshore wind capacity by the year 2045. In 2022 the Bureau of Ocean Energy Management (BOEM) held lease sales for two wind energy areas (WEAs) located in deeper shelf waters in central California and northern California with high-value power production potential (Wang et al., 2019, 2022). While recent policy developments have introduced uncertainty regarding the timing and extent of offshore wind development in some of the lease areas, parallel federal initiatives have renewed consideration of offshore oil and gas leasing in the same broader region (BOEM,

* Corresponding author.
E-mail address: rkwalter@calpoly.edu (R.K. Walter).

https://doi.org/10.1016/j.rsma.2026.105566
Received 27 May 2026; Received in revised form 9 October 2026; Accepted 16 October 2026
Available online 19 October 2026
2352-4855/© 2026 The Author(s). Published by Elsevier B.V. This is an open access article under the CC BY license (http://creativecommons.org/licenses/by/4.0/).

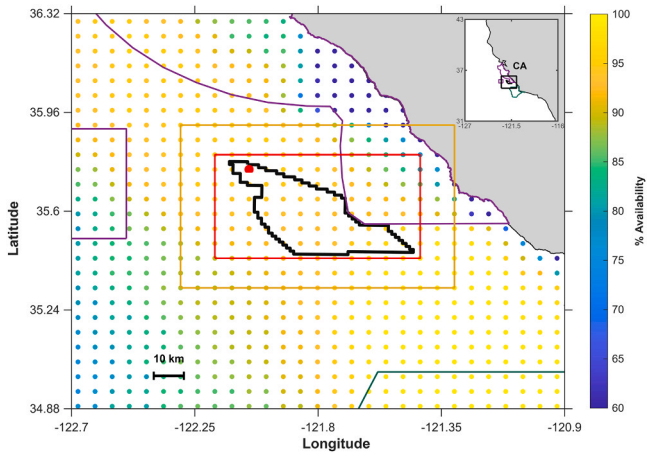


Fig. 1. Percent data availability for the 6 km surface current grid from 2012 to 2022 across the central California coast. The black outline denotes the offshore wind energy area (WEA), the red box denotes the region of interest for the Lagrangian coherent structure (LCS) analysis and FTLE fields, the orange box denotes the domain of influence that contains approximately 95% of the data used to calculate FTLEs in the red box, and the red dot denotes the location of an example time series of currents shown in Fig. 2. The purple (Monterey Bay) and teal (Chumash Heritage) lines denote the National Marine Sanctuary boundaries adjacent to the WEA. For HFR site locations see https://hfradar.ioos.us/hfrnet/.

2026). Although evolving, these potentially competing offshore interests highlight the need for a long-term baseline understanding of regional oceanographic conditions that can inform multiple development scenarios. For offshore wind development, the sites will require floating turbines, given the depth on the outer continental shelf. Floating turbines are a rapidly growing technology that may reduce impacts on human activities, while also capturing stronger and more consistent winds (Farr et al., 2021). With floating turbines, and similarly oil and gas development, there are also important environmental considerations for site planning and ongoing operations in deeper waters. These include changes to the physical environment and current patterns, impacts to the biological environment including higher trophic level species and fisheries, and the potential for pollutant and chemical spills, among others (Farr et al., 2021; Wang et al., 2022; Dalsin et al., 2025; Renner et al., 2025).

The proposed offshore energy development area and WEA are located on the outer continental shelf within the California Current. The California Current is an eastern boundary current that is among the most productive marine ecosystems in the world, supporting valuable fisheries and higher trophic level species (Pauly and Christensen, 1995; Wang et al., 2022). This productivity is partially fueled by atmospheric winds that drive the seasonal upwelling of nutrient-rich waters into coastal zones along a band that extends tens of kilometers from the coast typically during the spring and summer months (Checkley and Barth, 2009; García-Reyes and Largier, 2012; Walter et al., 2018). The California Current is a dynamic system shaped by spatiotemporal variability in surface currents where processes ranging from seasonal to submesoscale generate fronts, filaments, meanders, and eddies that impact critical ecosystem processes (Nidzieko and Largier, 2013; Kim et al., 2011; Payandeh et al., 2023).

To better understand complex flows, researchers have increasingly utilized Lagrangian coherent structures (LCS). LCS characterize robust material surfaces that exert a major influence on nearby trajectories over finite time intervals and play a critical role in organizing fluid motion and revealing coherent flow patterns (Peacock and Haller, 2013; Haller, 2015; Peng et al., 2024). They objectively identify patterns, such as eddies, fronts, filaments, or material lines of maximum convergence or divergence (“ridges”), by quantifying the Lagrangian deformation of particle trajectories over a finite time interval. The finite-time Lyapunov exponent (FTLE) is a widely used tool to approximate LCS (Shadden et al., 2005). FTLEs are computed from the largest eigenvalue of the Cauchy-Green strain tensor and quantify the rate of separation of nearby particle trajectories over a finite integration interval. Ridges in forward-time FTLE fields approximate repelling LCS and identify maximum stretching or divergence, while ridges in backward-time FTLE fields approximate attracting LCS and identify regions of maximum convergence. Regions with enhanced frontal activity (e.g., upwelling fronts, filaments, eddies, instabilities, etc.) often coincide with elevated FTLE values because these features are associated with enhanced stretching and transport barriers that separate distinct water masses (e.g., fronts).

Both forward-time repelling ridges and backward-time attracting ridges are ecologically relevant for offshore infrastructure applications. Attracting ridges can aggregate and concentrate plankton and organic matter by promoting convergence. These regions of elevated prey density can enhance predator foraging efficiency and success for higher trophic levels. This has been observed for valuable fish species and marine mammals, including whales (Harrison et al., 2013; Watson et al., 2018; Baudena et al., 2021; Fahlbusch et al., 2022, 2024; Veatch et al., 2025a). Thus, elevated attracting FTLE values are often useful indicators of biological hotspots. In contrast, repelling ridges enhance the separation of nearby trajectories and can promote larval dispersal, potentially increasing connectivity among populations.

Attracting and repelling LCS also identify barriers to contaminant dispersion and forecast pollutant transport, which is particularly relevant in regions where multiple offshore energy sources are being considered (Lekien et al., 2005; Olascoaga and Haller, 2012). Regions with many attracting ridges are sensitive to negative impacts from pollutant spills since pollutants will tend to converge and concentrate there. This convergence increases the potential for negative ecosystem impacts since the encounter rate between prey, predators, and pollutants is higher, but it may offer advantages in cleanup efforts given the concentration to a smaller and more defined area. Repelling ridges, on the other hand, are regions where pollutant dispersal will be locally maximum and lead to more difficult cleanup efforts. Thus, LCS (and the FTLE fields identifying them) have emerged as a critical tool for elucidating complex fluid patterns and providing an important understanding of how hidden flow structures can impact marine ecosystems (Peng et al., 2024). Here, we quantify both attracting and repelling FTLEs since they may both be of interest to different stakeholders, marine spatial planning objectives, and scenario planning exercises.

A recent study examined seasonal variability in FTLE fields using multi-year surface current records derived from high-frequency radar (HFR) networks (Veatch et al., 2025b). They quantified seasonal variability in attracting FTLE fields in the Mid-Atlantic Bight, showing enhanced attracting features during the spring and summer seasons. Building on this framework, we examine both attracting and repelling FTLE fields in the California Current in the vicinity of a proposed offshore energy development region. Using more than a decade (2012–2022) of high-frequency radar observations, we quantify persistent seasonal patterns in surface currents and FTLE fields in and around the central California outer shelf region. Rather than identifying individual transient LCS events, our objective is to characterize recurring seasonal patterns in attracting and repelling transport structures over the available observational record. We then examine the implications of these seasonal patterns for ecosystem dynamics, pollutant transport, and marine spatial planning.

2. Methods

2.1. Wind Energy Area (WEA)

The central California region is located in the highly productive California Current. In 2022, BOEM held a successful lease sale for an

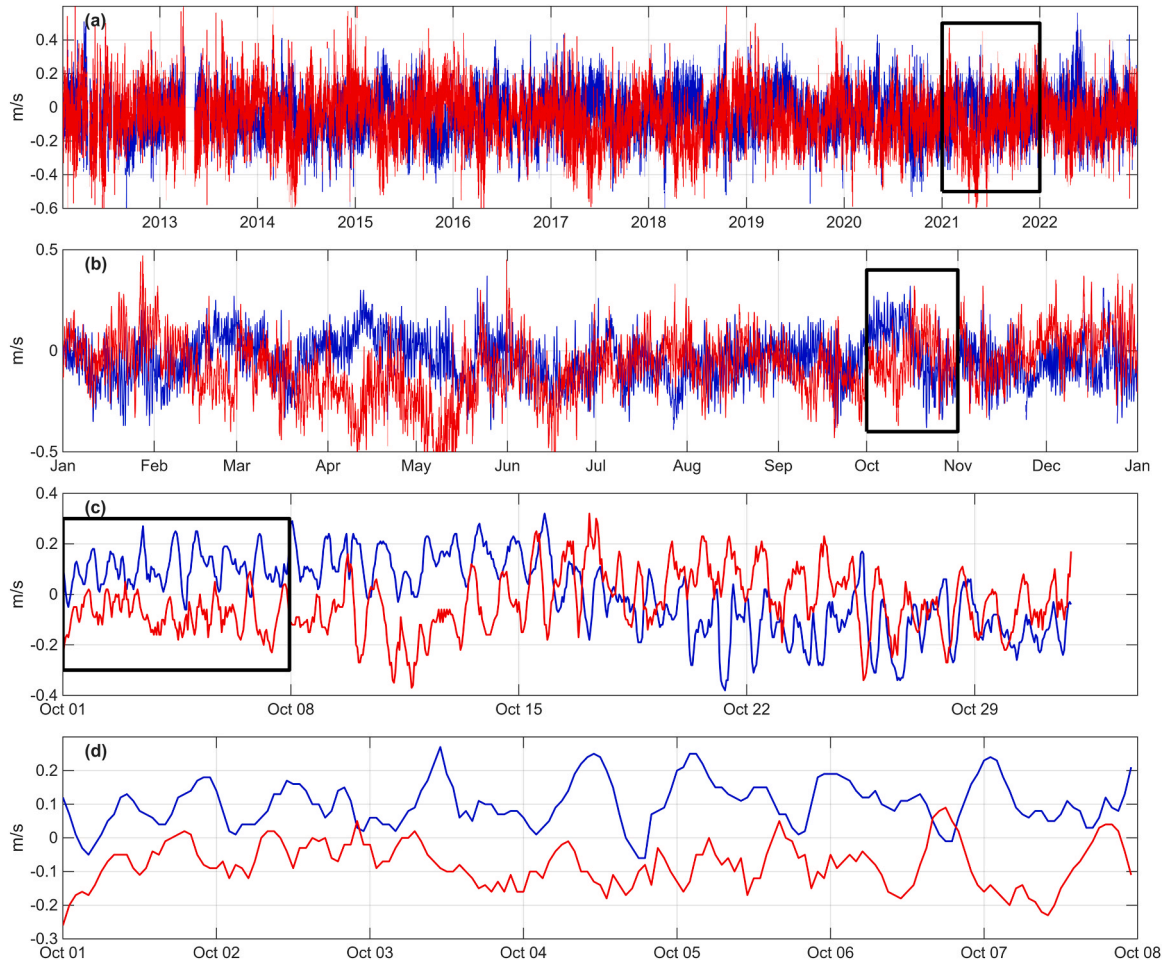


Fig. 2. Example time series showing the east-west (blue, positive east) and north-south (red, positive north) velocity components from the northwest corner of the wind energy area (WEA, red dot shown in Fig. 1). Panel (a) shows the entire record from 2012 to 2022, while each subsequent panel shows zoomed in regions during the time period denoted in the black box. For example, panel (b) shows the annual time series from 2021 (zoom in of the black box in panel (a)).

offshore WEA tens of kilometers off the central California coast (Fig. 1), with plans for the future development of hundreds of floating offshore wind turbines (Wang et al., 2022). This region is located adjacent to two national marine sanctuaries in the Monterey Bay National Marine Sanctuary and the newly designated Chumash Heritage National Marine Sanctuary. Moreover, the area supports a high diversity and abundance of marine mammals, including numerous whale species, that feed and migrate in the highly productive area (Calambokidis et al., 2024). This region is also home to numerous high-value fisheries (Wang et al., 2022, 2024). Recent policy developments in the United States have introduced uncertainty regarding offshore wind energy development and timelines in this region; however, the broader continental shelf region remains an active area of consideration for development of multiple offshore energy sectors, including offshore wind, oil, and gas (BOEM, 2026).

2.2. *High-frequency radar (HFR) surface current data*

A network of high-frequency radars along the central California coast produces hourly maps of surface currents spanning several hundred kilometers from the coast with a horizontal resolution on the order of kilometers. The network along the California coast is one of the longest and most complete coastal surface current datasets in the world, providing accurate long-term measurements of spatial variability at a relatively high resolution, both temporally (hourly) and spatially (6 km used here) (Paduan and Washburn, 2013). This technology uses Doppler backscatter in the high-frequency portion of the electromagnetic spectrum to produce radial velocities at a single radar site, with two or more sites combining to create total vector products. HFR-derived surface currents have been validated with surface currents measured using several other approaches (see Review by Paduan and Washburn, 2013 and the references therein). We utilized hourly data from the 6 km product from 2012 through 2022 in a bounding box surrounding the WEA (Fig. 1; data available at https://www.ncei.noaa.gov/thredds-ocean/catalog/ioos/hfradar/rtv/catalog.html). Fig. 1 shows the percent availability of hourly data across the central California region. For quantifying variability across months, we calculated monthly mean current vectors at each location across all respective months over more than a decade of data. We also computed current ellipses at each location across each respective month by performing a principal axes analysis at each location and plotting major and minor axes as ellipses. These ellipses denote how the variance in the magnitude and direction of surface currents at each location changes across different months of the year.

2.3. *Lagrangian coherent structures*

2.3.1. *LCS toolbox*

We identified LCS by calculating FTLE fields using HFR data and the widely utilized LCS Tool in MATLAB (Onu et al., 2015). The toolbox calculates FTLE fields by numerically integrating particle trajectories through a time-dependent velocity field. The toolbox uses a regular grid of initial particle positions and computes the flow map, which describes

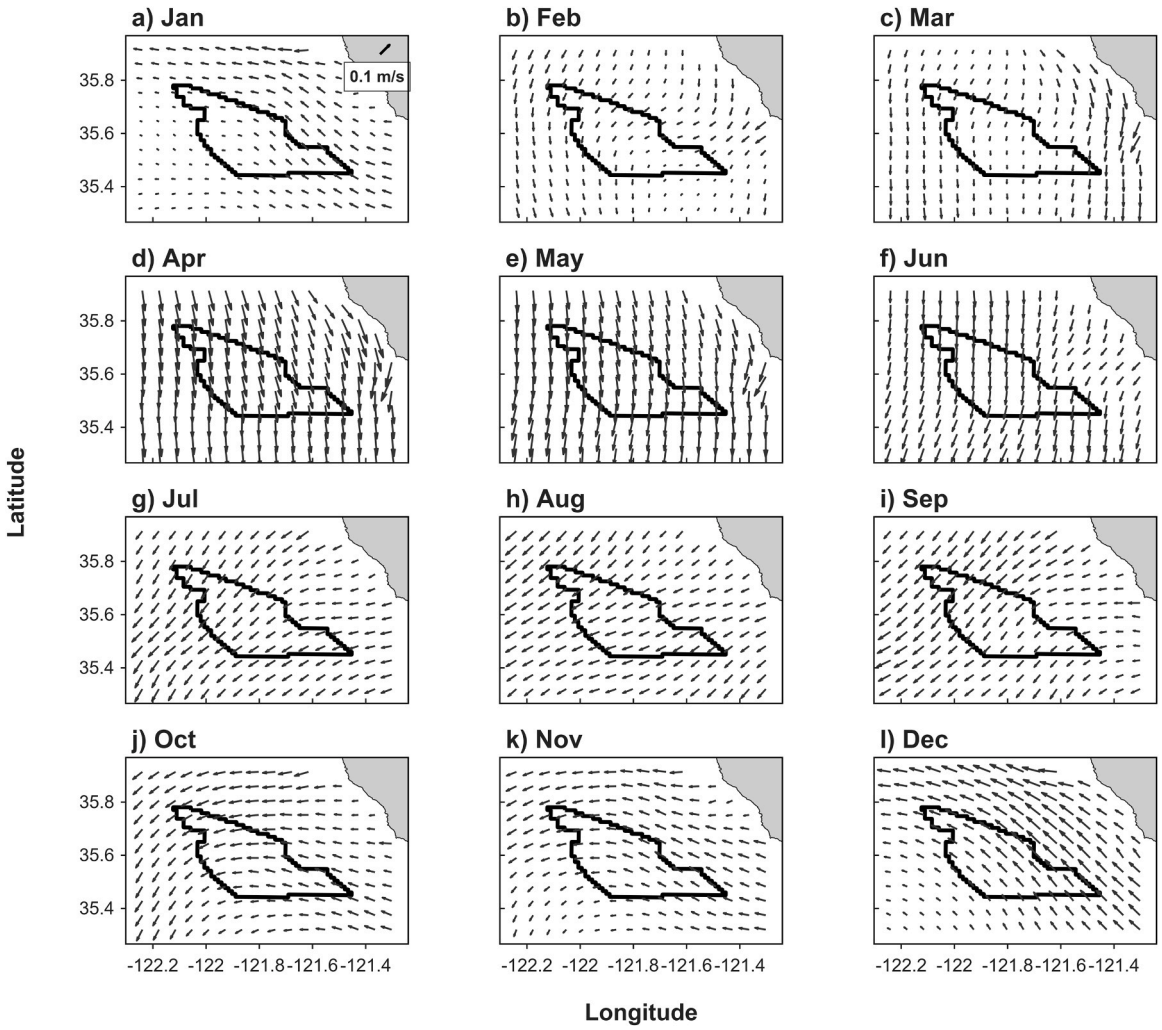


Fig. 3. Monthly mean current vectors over the entire record from 2012 to 2022 in and around the central California wind energy area (WEA). The black outline denotes the offshore WEA. A scale quiver is shown in panel (a).

the displacement of each particle from its initial position to its final position over a finite time integration window. Spatial gradients of the flow map are used to calculate the Cauchy-Green strain tensor, whose eigenvalues and eigenvectors characterize the deformation of fluid parcels. The largest eigenvalue (λ_{max}) of the Cauchy-Green strain tensor (C) is used to compute the FTLE over the integration window (T):

$$FTLE(\boldsymbol{x}_o, t_o, T) = \frac{1}{2|T|}\ln\lambda_{\max}(\mathrm{C}(\mathbf{x}_o, t_o)) \quad . \tag{1}$$

FTLE fields were calculated by releasing particles at a spatial resolution of approximately 600 m (e.g., 10x the native ~6 km resolution of the HFR product) following established methods (Shadden et al., 2009; Fahlbusch et al., 2022). Following Fahlbusch et al. (2022) from a nearby region, we utilized a 48 hr integration period for FTLE calculations, a time period that minimizes the influence of tidal currents and captures transport structures in the vicinity of the WEA and area of interest here. A timescale choice of 48 hr is also relevant for rapid operational response in the case of pollutant spills like oil, and this timescale also had the best correlations with blue whale foraging patterns in the Santa Barbara Channel (Fahlbusch et al., 2022). We also tested integration times of 1 and 3 days and found that major results and general patterns were not sensitive to these integration times.

2.3.2. Particle tracking runs

To alleviate spurious FTLE fields as a result of missing HFR data, and avoid introducing artifacts from interpolation schemes, we first ran particle tracking runs to determine a domain of influence over which to assess HFR data availability for inclusion in FTLE calculations. This domain of influence represents the spatial region over which particle trajectories influence FTLE fields inside of the WEA and region of interest (Fig. 1). Cumulative Lagrangian particle trajectories and positions were calculated using the LCS Tool over 48 hr windows continuously over the entire time period for both forward and backward in time runs. Particles were released inside of the WEA (red box, Fig. 1) to visualize the spatial region over which velocity fields influence particle trajectories that originate inside of the WEA. The domain of influence was selected because it contained approximately 95% of the hourly particle positions over the entire record from 2012 to 2022 (see Section 3.2).

2.3.3. FTLE fields and seasonal patterns

We used the particle release experiments described above to determine the 48 hr runs over which FTLE fields would be computed. Given the interest in features inside of the WEA (red box, Fig. 1), we used a threshold criterion of 95% HFR data availability within the domain of influence (orange box, Fig. 1) defined by the particle tracking runs to determine 48 hr integration time periods over which to calculate FTLE fields. FTLE calculations require a dataset with no missing velocity data. Points with small amounts of missing data predominantly at edge boundaries were interpolated using nearest neighbor to avoid introducing non-physical artifacts. We found that major results were not

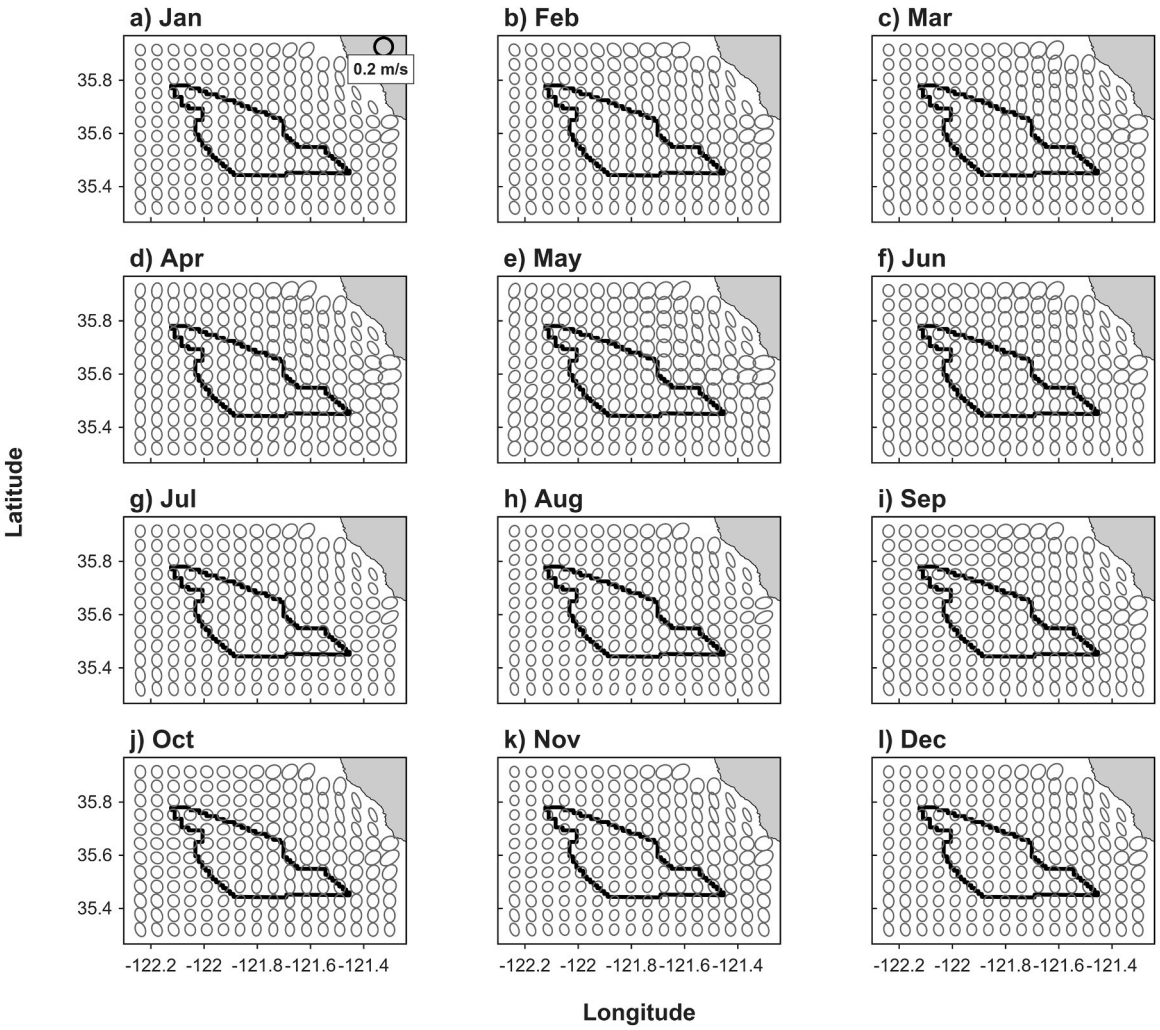


Fig. 4. Monthly principal axes current ellipses over the entire record from 2012 to 2022 in and around the central California wind energy area (WEA). The black outline denotes the offshore WEA. A scale ellipse is shown in panel (a).

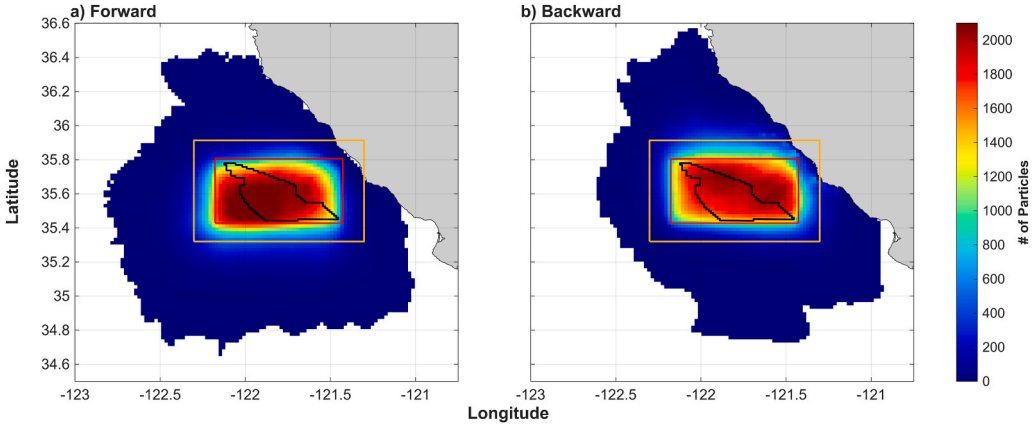


Fig. 5. Cumulative particle trajectories highlighting the number of particles in a given grid cell at any point during each 48 hr run, summed over the entire record from 2012 to 2022. Particle positions are quantified in a grid with horizontal spatial dimensions of approximately 2 km (0.02° in both directions) for visual representation. The black outline denotes the offshore wind energy area (WEA), the red box denotes the region of interest for the Lagrangian coherent structure (LCS) analysis (FTLE fields), and the orange box denotes the domain of influence in which particle trajectories inside this box exert a major influence on the calculation of FTLE values in the red box.

sensitive to the 95% availability threshold. Following this, FTLE fields were computed over 48 hr windows over the entire 11 years for both forward and backward runs in which there was 95% data availability in the domain of influence determined from the particle tracking runs. These individual FTLE fields computed over 48 hr windows (see Figure S1 for examples) were then used to create monthly composite

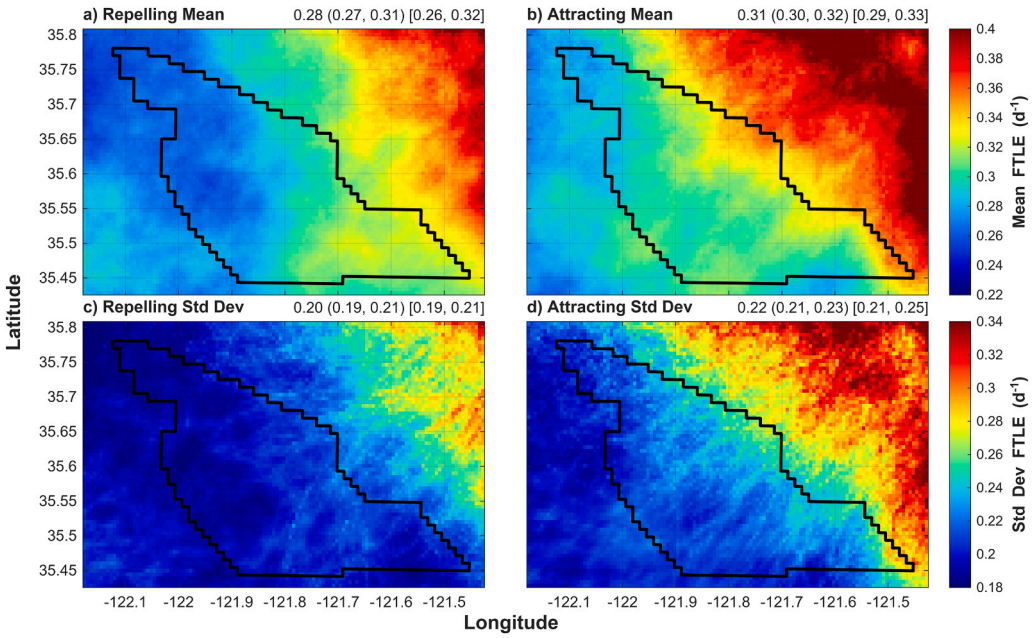


Fig. 6. Mean and standard deviation of finite-time Lyapunov exponent (FTLE) fields calculated using 48 hr integration windows over the entire record from 2012 to 2022 for both forward [repelling ridges, panels (a) and (c)] and backward [attracting ridges, panels (b) and (d)] in time. Spatial statistics of FTLE values within the WEA (black outline) are reported in the top right of each panel using the format: median (25th percentile, 75th percentile) [10th percentile, 90th percentile].

averages. Monthly composite averages were calculated by averaging the 48 hr FTLE fields over each month of the year over the full dataset (e.g., all January FTLE values over all 11 years, etc.), and the variability was determined from the standard deviation. Finally, spatial statistics (median, 10th, 25th, 75th, and 90th percentile) of FTLE values inside of the WEA were calculated.

2.4. Coastal upwelling transport index

The coastal upwelling transport index (CUTI) was utilized to assess seasonal patterns in coastal upwelling and potential linkages with seasonal FTLE patterns. The CUTI index provides a measure of vertical transport near the coast, driven by Ekman transport, wind-stress curl driven upwelling, and cross-shelf geostrophic transport in one-degree latitude bins extending 75 km offshore (Jacox et al., 2018). We utilized the monthly CUTI index at a latitude of 35°N, which encompassed the study region (data available at https://mjacox.com/upwelling-indices/). We calculated monthly composite CUTI averages from 2012 to 2022 and compared them with the spatial median of the monthly mean FTLE fields inside of the WEA.

3. Results

3.1. Surface current seasonal patterns

The surface currents in this region are characterized by variability across a range of scales, including seasonal changes, synoptic-scale variability (1–2 week cycles), and higher-frequency (diurnal and semi-diurnal) variability (Fig. 2). The seasonal mean current structure shows relatively weak (~0.05 m/s) currents during the winter months (Jan-Mar), with currents moving poleward and to the northwest (approximately parallel to the coast) in December and January (Fig. 3a-c). There is an abrupt transition to strong equatorward currents in April and May (~0.15 m/s), with some of the strongest currents observed during the annual cycle during this spring transition (Fig. 3d-e). Moving into the summer months and persisting through the early fall, the currents weaken slightly (~0.10 m/s) and start to veer offshore and towards the southwest (Fig. 3f-j). Starting in late fall, the currents transition to moving offshore (towards the west) and eventually turn to move poleward (towards the northwest) heading into December (Fig. 3k-l).

The current ellipses displayed variability across all months of the year in and around the WEA (Fig. 4). Along the coastal boundary, current ellipses were more polarized and oriented parallel to the coast. There was typically greater variance in currents during the spring and early summer months (e.g., major axis magnitude of ~0.14 m/s in winter months versus ~0.16 m/s in April to June), indicated by larger current ellipses, especially in the region between the coastline and the WEA (Fig. 4d-f).

3.2. Particle tracking

The position of particles released every 48 hr in the WEA summed over the entire record from 2012 to 2022 is shown in Fig. 5. The domain of influence (orange box, Fig. 5) over which particle trajectories have a major influence on FTLE calculations inside of the WEA (red box, Fig. 5) captured 94.54% of the particle positions for forward in time (Figs. 5a) and 94.67% for backward in time (Fig. 5b), indicating that FTLE calculations are most sensitive to data availability within this domain.

3.3. FTLE seasonal patterns

Mean FTLE fields over the entire time period were substantially larger near the coast (~0.35–0.40 d^{-1}) compared to farther offshore inside of the WEA (~0.20–0.35 d^{-1}) for both forward-time (repelling ridges) and backward-time (attracting ridges) runs (Fig. 6). The attracting ridges generally had larger mean values extending farther from the coastline, with moderate values (~0.35 d^{-1}) calculated along the eastern edges of the middle and southern portions of the WEA and a spatial median in the WEA of 0.31 d^{-1} (Fig. 6c). Repelling ridge FTLE values were minimal throughout the entire WEA (spatial median of 0.28 d^{-1}) except for moderate values (~0.30–0.35 d^{-1}) in the southeastern corner (Fig. 6a). The standard deviation of the FTLE field generally mirrored the mean patterns, with large variability in FTLE fields closer to the coastline and outside of the WEA (up to ~0.35 d^{-1}) and moderate variability (~0.25 d^{-1}) extending into the eastern edges of the WEA (Figs. 6b and 6d).

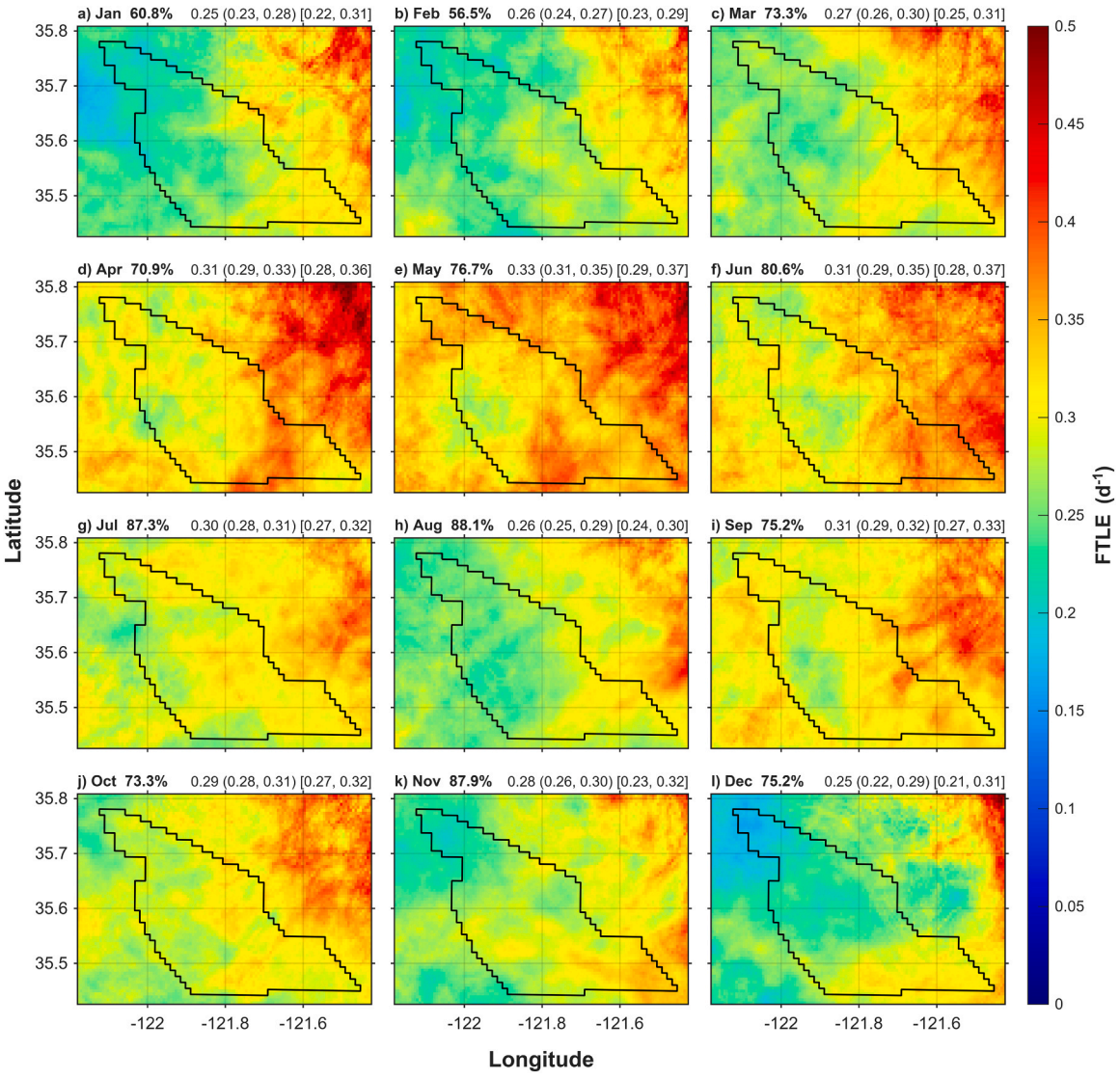


Fig. 7. Monthly mean of finite-time Lyapunov exponent (FTLE) fields calculated using 48 hr integration windows over the entire record from 2012 to 2022 for forward in time runs (repelling ridges). The percentages in each label denote the percentage of 48 hr integration windows in which the data availability in the domain of influence exceeded the 95% data threshold for each respective month and were included in the FTLE calculations (Fig. 5). The black outline denotes the offshore wind energy area (WEA). Spatial statistics of FTLE values within the WEA (black outline) are reported in the top right of each panel using the format: median (25th percentile, 75th percentile) [10th percentile, 90th percentile].

The forward in time (repelling ridges) FTLE fields showed distinct monthly changes (Fig. 7). During the winter months (Dec-Feb), FTLE values were minimal inside of the WEA (spatial median of 0.25 d^{-1} in January), with moderate FTLE values (~0.4 d^{-1}) closer to the coast. Starting in March and extending through the spring and early summer months, FTLE values near the coast increased substantially to the largest values observed over the year (~0.5 d^{-1}). Inside of the WEA, FTLE values increased substantially (spatial median of ~0.33 d^{-1} in May), especially in the southeastern region (~0.4 d^{-1}). May showed the greatest mean FTLE fields throughout most of the WEA. In the late summer months, the FTLE values inside of the WEA started to decrease into the fall months (spatial median of 0.3 d^{-1} in July), with moderate patches of elevated FTLE values observed throughout the southeastern corner. The monthly standard deviation values for the forward in time FTLE (Fig. 8) largely mirrored the seasonal variability in the mean fields. In general, the standard deviation was higher closer to the coastline (up to ~0.4 d^{-1} in winter), with increased variability during the spring and early summer months. Variability inside of the WEA also peaked in these months (spatial median of ~0.17 d^{-1} in January versus 0.23 d^{-1} in May).

The backward in time (attracting ridges) FTLE fields also displayed a distinct seasonality and pattern of increasing FTLE values during the spring and early summer months and closer to the coastline (Fig. 9). In general, there were larger mean FTLE values that extended into the WEA during the fall and winter months compared to the repelling ridges (spatial median of 0.25 d^{-1} for repelling versus 0.29 d^{-1} for attracting in January). During the spring and summer months, FTLE fields increased substantially closer to the coastline and inside of the WEA (spatial median of 0.29 d^{-1} in January versus 0.34 d^{-1} in May). The elevated mean values also extended throughout nearly the entire WEA domain, especially in April and May (e.g., 90th percentile of 0.39 d^{-1} for attracting versus 0.36 d^{-1} for repelling in April). Whereas there were typically larger mean FTLE values in the southeastern corner of the WEA in a given month for the forward in time (repelling ridges), the middle edge of the WEA closest to the coastline generally displayed the largest values (~0.40–0.45 d^{-1}) in a given month for the backward in time (attracting ridges) runs, which is also captured in the mean FTLE fields over all time (Fig. 6). The variability of the backward in time FTLE fields, as measured

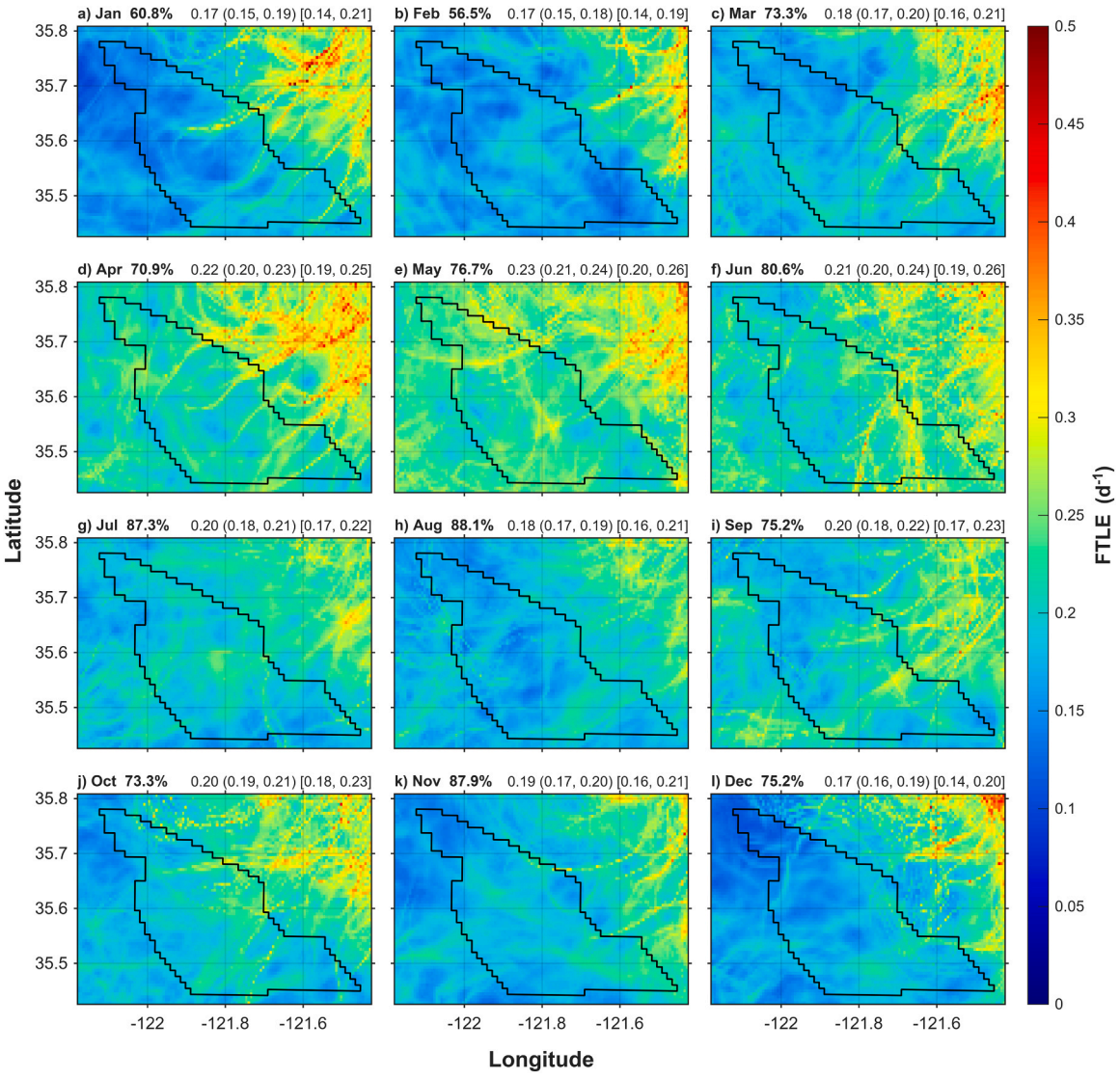


Fig. 8. Monthly standard deviation of finite-time Lyapunov exponent (FTLE) fields calculated using 48 hr integration windows over the entire record from 2012 to 2022 for forward in time runs (repelling ridges). The percentages in each label denote the percentage of 48 hr integration windows in which the data availability in the domain of influence exceeded the 95% data threshold for each respective month and were included in the FTLE calculations (Fig. 5). The black outline denotes the offshore wind energy area (WEA). Spatial statistics of FTLE values within the WEA (black outline) are reported in the top right of each panel using the format: median (25th percentile, 75th percentile) [10th percentile, 90th percentile].

by the monthly standard deviation, also showed enhanced variability in the spring and summer months extending into the WEA (spatial median of 0.20 d^{-1} in January versus 0.25 d^{-1} in May; Fig. 10).

The seasonal evolution of both repelling and attracting FTLE fields within the WEA was broadly consistent with the Coastal Upwelling Transport Index (CUTI; Fig. 11). Composite monthly CUTI values increased during the spring and early summer and declined through the fall months until reaching winter minima, which was generally consistent with seasonal changes in the spatial median of the monthly mean FTLE fields inside of the WEA (Fig. 11).

4. Discussion and conclusions

In this contribution, we analyzed over a decade of surface currents from a network of high-frequency radars to characterize mean current patterns and transport structures, derived from a Lagrangian coherent structure analysis, in and around a proposed offshore wind energy region along the outer continental shelf of central California. We found a strong seasonal cycle in both the mean Eulerian (Fig. 3) and Lagrangian (Figs. 7 and 9) flow fields. During the spring months, there was an abrupt transition from generally weak poleward flows (~0.05 m/s) observed during the winter months to more intensified equatorward flows (~0.15 m/s) (Fig. 3). This time period also coincided with a large increase in both forward in time (repelling ridges, Fig. 7) and backward in time (attracting ridges, Fig. 9) mean FTLE fields closer to the coastline, with increased FTLE values also extending into the WEA (e.g., within WEA, spatial median FTLE values increased by 32% for repelling ridges and 17% for attracting ridges between January and May). Both forward and backward in time runs showed distinct spatial differences between repelling and attracting fields, respectively, with stronger repelling ridges in the southeastern corner (~0.4 d^{-1}) and stronger attracting ridges in the center edge of the WEA (~0.40–0.45 d^{-1}) closest to the coastline (Figs. 6, 7, and 9). In general, attracting FTLE fields exhibited stronger values and a broader spatial extent inside of the WEA (spatial median of 0.31 d^{-1}) compared to repelling FTLE fields (spatial median of 0.28 d^{-1}), suggesting potential for increased material aggregation across this region.

The seasonality of the mean surface currents and enhanced transport

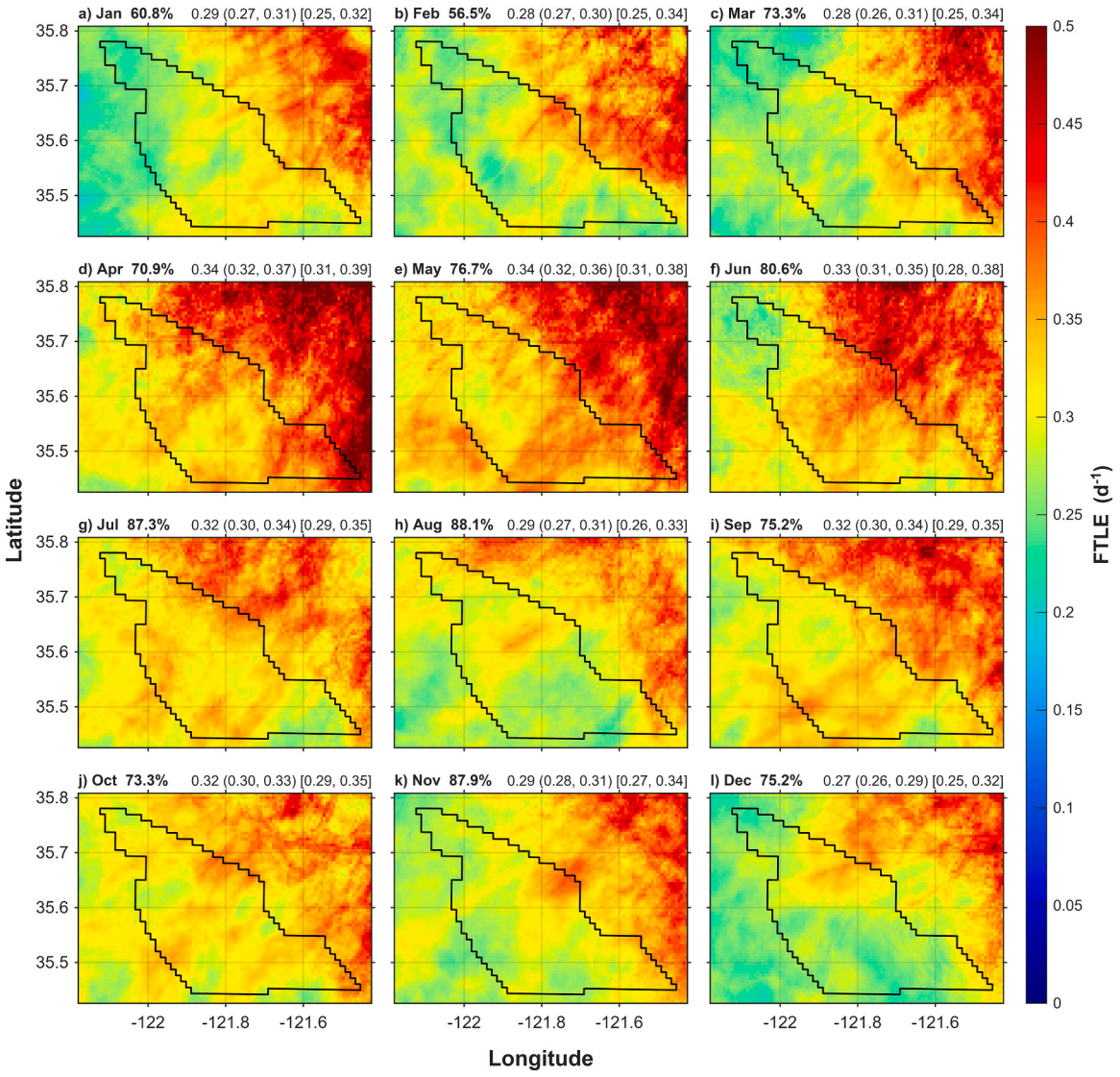


Fig. 9. Monthly mean of finite-time Lyapunov exponent (FTLE) fields calculated using 48 hr integration windows over the entire record from 2012 to 2022 for backward in time runs (attracting ridges). The percentages in each label denote the percentage of 48 hr integration windows in which the data availability in the domain of influence exceeded the 95% data threshold for each respective month and were included in the FTLE calculations (Fig. 5). The black outline denotes the offshore wind energy area (WEA). Spatial statistics of FTLE values within the WEA (black outline) are reported in the top right of each panel using the format: median (25th percentile, 75th percentile) [10th percentile, 90th percentile].

structures, and in particular the increases observed during the spring and summer months, is consistent with the well-established dynamics of the California Current upwelling system (Strub et al., 1987; Strub and James, 2000; Checkley and Barth, 2009; García-Reyes and Largier, 2012). The spring and summer upwelling season was also characterized by a sharp increase in both attracting and repelling FTLE fields in and around the proposed wind energy development region, particularly near the coastline (Figs. 7 and 9). These seasonal patterns are consistent with recent observations from the Mid-Atlantic Bight from Veatch et al. (2025b) that also reported enhanced attracting FTLE features in the spring and summer due to seasonal stratification. The spatial gradients and seasonal timing in FTLE magnitude in this study likely reflect the influence of upwelling-driven dynamics (intensified currents, fronts, filaments, eddies, and instabilities that drive substantial horizontal stirring) within a coastal band that extends tens of kilometers from the coastline (see Fig. 11; Strub et al., 1991; Castelao et al., 2006; Capet et al., 2008; Nidzieko and Largier, 2013; Kessouri et al., 2020). The extension of elevated FTLE signals away from the coastline and into the proposed wind energy area during the upwelling season highlights the importance of the offshore extension and spatiotemporal variability of these dynamic features.

One potential uncertainty is that the 6 km horizontal resolution of the HFR product may not fully resolve smaller submesoscale processes and their associated stirring. Moreover, in addition to the seasonal variability documented here, intraseasonal and synoptic-scale variability in the upwelling wind forcing (e.g., upwelling-relaxation cycles, Trautman and Walter, 2021) is also likely important in governing the dynamics of particle aggregation, separation rates, and the evolution of FTLE fields. While the goal of the present study is to establish seasonal patterns using more than a decade of observations, a more dynamical approach that explicitly examines the evolution of FTLE fields under different wind-forcing regimes and during individual events would provide additional insight into the physical mechanisms governing transport structure formation. Future work should also investigate temporal trends (see Figure S2 for a time series of FTLE fields) and interannual variability, as well as the response of FTLE fields to extreme events (anomalous upwelling, storms, etc.).

The seasonal and spatial patterns in FTLE fields also shape potential

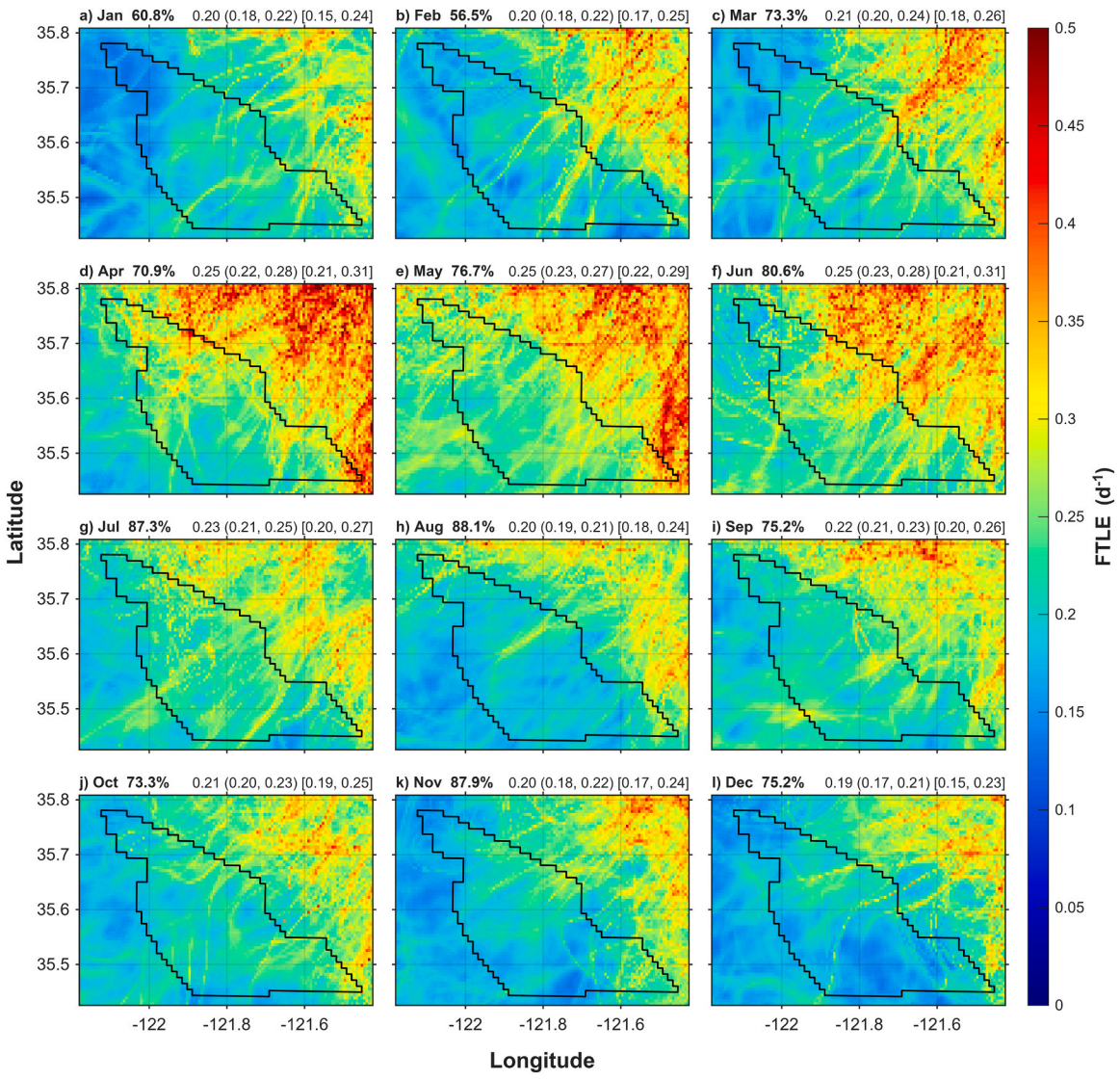


Fig. 10. Monthly standard deviation of finite-time Lyapunov exponent (FTLE) fields calculated using 48 hr integration windows over the entire record from 2012 to 2022 for backward in time runs (attracting ridges). The percentages in each label denote the percentage of 48 hr integration windows in which the data availability in the domain of influence exceeded the 95% data threshold for each respective month and were included in the FTLE calculations (Fig. 5). The black outline denotes the offshore wind energy area (WEA). Spatial statistics of FTLE values within the WEA (black outline) are reported in the top right of each panel using the format: median (25th percentile, 75th percentile) [10th percentile, 90th percentile].

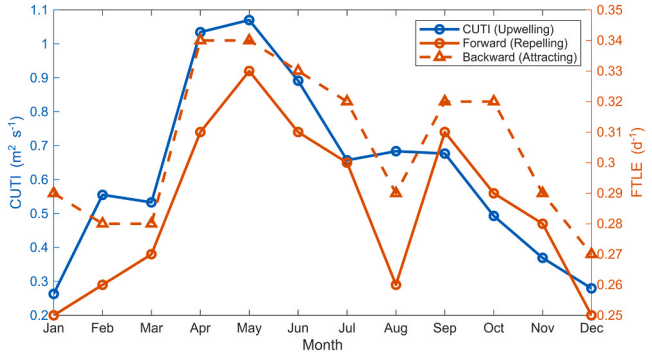


Fig. 11. Composite average of monthly upwelling index (CUTI) values from 2012 to 2022 (left axis, blue) and the spatial median of the monthly mean FTLE values inside of the WEA for the forward (repelling, right axis, red solid) and backward (attracting, right axis, red dashed) in time runs over 2012–2022, as in Figs. 7 and 9, respectively.

ecological responses in this region. The seasonal intensification of attracting ridges during the spring and summer upwelling season also aligns with periods of peak biological productivity in the California Current System, as the upwelling of nutrient-rich subthermocline waters fuels productivity along the coast (Checkley and Barth, 2009; Walter et al., 2018; Barth et al., 2020; Fig. 11). This correspondence suggests that the observed transport structures may contribute to organizing prey fields and shaping the spatial structure of marine food webs in the region (e.g., Veatch et al., 2025a). It is important to note that the attracting FTLE fields exhibited spatial variability within the WEA, especially along the eastern boundary, suggesting that ecological impacts may not be uniform across the WEA. In contrast, repelling ridges enhance the stretching and dispersal of water parcels and may indirectly influence primary productivity through transport and filamentation rather than by localized biological aggregation as in attracting ridges. The extension of moderate to strong attracting FTLE ridges into portions of the WEA during this biologically active upwelling season highlights that the WEA may overlap with ecologically important aggregation and feeding zones for higher trophic level migratory species including whales and pelagic

fisheries (Fahlbusch et al., 2022; Watson et al., 2018). Future work should incorporate spatiotemporal data layers on both fishing effort (e.g., Wang et al., 2024) and whale tagging data (e.g., Calambokidis et al., 2024) to further assess the relationship between attracting FTLE fields and whale migration patterns (Fahlbusch et al., 2022) and fisher behavior in the vicinity of the WEA (Watson et al., 2018).

The development of seasonal patterns of both attracting and repelling FTLE values provides a valuable framework for assessing environmental risks associated with potential offshore wind energy development, operations, and maintenance. The observed seasonal strengthening of both attracting and repelling FTLE fields suggests that the transport and fate of pollutants may vary substantially throughout the year, with stronger aggregation and dispersal processes occurring during the spring and summer upwelling season. These seasonal patterns have direct implications for the timing of construction, maintenance, and operational activities, as these activities could be scheduled to minimize overlap with times of enhanced ecological vulnerability. More broadly, the integration of LCS analyses into marine spatial planning exercises may allow for the incorporation of dynamic oceanographic information into future siting decisions and buildout scenarios. Future work could also integrate these LCS analyses into ecosystem models of fisheries and whale migration pathways to improve predictions of species distributions and help inform management actions, such as reducing the risk of whale strikes. Together, these applications could enable a more thorough evaluation of trade-offs between renewable energy development and ecosystem conservation, providing a framework that can be applied to other regions where offshore energy and other emerging blue economy activities are being considered (White et al., 2024).

This study takes advantage of more than a decade of high-resolution (6 km) surface current observations to evaluate the seasonal and spatial evolution of FTLE fields on the outer continental shelf of central California, providing a critical baseline for assessing potential environmental change associated with future offshore energy developments, as well as broader shifts in upwelling systems under climate change (Bograd et al., 2023). The growing national and international HFR network continues to enable the observation of dynamic surface processes in the ocean at unprecedented spatial and temporal scales (Paduan and Washburn, 2013; Roarty et al., 2019). Building on this capability, the Lagrangian coherent structures derived from these long-term observations provide a framework for characterizing seasonal transport patterns relevant to ecosystem dynamics and environmental risk assessment (pollutant transport, search and rescue, etc.). The seasonal patterns developed here represent a scalable framework for supporting marine spatial planning and sustainable ocean use in a rapidly evolving Blue Economy.

CRediT authorship contribution statement

Ryan K. Walter: Writing – review & editing, Writing – original draft, Validation, Supervision, Project administration, Methodology, Funding acquisition, Formal analysis, Data curation, Conceptualization. **Paul Choboter:** Writing – review & editing, Writing – original draft, Validation, Supervision, Project administration, Methodology, Formal analysis, Conceptualization. **Andres E. Rocha Jayasinha:** Writing – review & editing, Validation, Methodology, Formal analysis. **Rapha Coutin:** Writing – review & editing, Validation, Methodology, Formal analysis. **Corbin Luoma:** Writing – review & editing, Methodology, Formal analysis. **Leah Hoogstra:** Writing – review & editing, Methodology, Formal analysis. **Casper Pratt:** Writing – review & editing, Methodology, Formal analysis. **Mazen Idriss:** Writing – review & editing, Methodology, Formal analysis. **Emmett Ehrnstein:** Writing – review & editing, Formal analysis. **Ian Robbins:** Writing – review & editing, Data curation.

Declaration of Competing Interest

The authors declare that they have no known competing financial interests or personal relationships that could have appeared to influence the work reported in this paper

Acknowledgements

We acknowledge support from the NOAA IOOS program through CeNCOOS (NOAA Award #NA21NOS0120090) and SCCOOS (NOAA Award #NA21NOS0120088) for the high-frequency radar measurements used in this study. Additional student support was provided by the William and Linda Frost Fund at Cal Poly, as well as the Santa Rosa Creek Foundation at Cal Poly. The suggestions from three anonymous reviewers greatly improved the manuscript.

Appendix A. Supporting information

Supplementary data associated with this article can be found in the online version at doi:10.1016/j.rsma.2026.105566.

Data availability

HFR data are available at the link provided in the manuscript

References

Barth, A., Walter, R.K., Robbins, I., Pasulka, A., 2020. Seasonal and interannual variability of phytoplankton abundance and community composition on the Central Coast of California. Mar. Ecol. Prog. Ser. 637, 29–43. https://doi.org/10.3354/meps13245.

Baudena, A., Ser-Giacomi, E., D'Onofrio, D., Capet, X., Cotté, C., Cherel, Y., D'Ovidio, F., 2021. Fine-scale structures as spots of increased fish concentration in the open ocean. Sci. Rep. 11. https://doi.org/10.1038/s41598-021-94368-1.

Bograd, S.J., Jacox, M.G., Hazen, E.L., Lovecchio, E., Montes, I., Buil, M.P., Shannon, L. J., Sydeman, W.J., Rykaczewski, R.R., 2023. Climate change impacts on eastern boundary upwelling systems. Annu. Rev. Mar. Sci. 15, 303–328. https://doi.org/10.1146/annurev-marine-032122-021945.

Bureau of Ocean Energy Management (BOEM), 2026. California oil and gas leasing activities. U.S. Department of the Interior.

Calambokidis, J., Kratofil, M.A., Palacios, D.M., Lagerquist, B.A., Schorr, G.S., Hanson, M.B., Baird, R.W., Forney, K.A., Becker, E.A., Rockwood, R.C., Hazen, E.L., 2024. Biologically Important Areas II for cetaceans within U.S. and adjacent waters - West Coast Region. Front. Mar. Sci. 11. https://doi.org/10.3389/fmars.2024.1283231.

Capet, X., McWilliams, J.C., Molemaker, M.J., Shchepetkin, A.F., 2008. Mesoscale to submesoscale transition in the California Current system. Part I: Flow structure, eddy flux, and observational tests. J. Phys. Oceanogr. 38, 29–43. https://doi.org/10.1175/2007JPO3671.1.

Castelao, R.M., Mavor, T.P., Barth, J.A., Breaker, L.C., 2006. Sea surface temperature fronts in the California Current System from geostationary satellite observations. J. Geophys. Res. Oceans 111. https://doi.org/10.1029/2006JC003541.

Checkley, D.M., Barth, J.A., 2009. Patterns and processes in the California Current System. Prog. Oceanogr. 83, 49–64. https://doi.org/10.1016/j.pocean.2009.07.028.

Dalsin, M., Walter, R.K., Mazzini, P.L.F., 2025. Offshore wind farms could impact coastal marine heatwaves in eastern boundary upwelling systems. Estuar. Coast. Shelf Sci. 313. https://doi.org/10.1016/j.ecss.2024.109102.

Fahlbusch, J.A., Cade, D.E., Hazen, E.L., Elliott, M.L., Saenz, B.T., Goldbogen, J.A., Jahncke, J., 2024. Submesoscale coupling of krill and whales revealed by aggregative Lagrangian coherent structures. Proc. R. Soc. B Biol. Sci. 291. https://doi.org/10.1098/rspb.2023.2461.

Fahlbusch, J.A., Czapanskiy, M.F., Calambokidis, J., Cade, D.E., Abrahms, B., Hazen, E. L., Goldbogen, J.A., 2022. Blue whales increase feeding rates at fine-scale ocean features. Proc. R. Soc. B Biol. Sci. 289. https://doi.org/10.1098/rspb.2022.1180.

Farr, H., Ruttenberg, B., Walter, R.K., Wang, Y.H., White, C., 2021. Potential environmental effects of deepwater floating offshore wind energy facilities. Ocean. Coast. Manag. 207. https://doi.org/10.1016/j.ocecoaman.2021.105611.

García-Reyes, M., Largier, J.L., 2012. Seasonality of coastal upwelling off central and northern California: New insights, including temporal and spatial variability. J. Geophys. Res. https://doi.org/10.1029/2011JC007629.

Global Wind Energy Council (GWEC), 2025. Global Wind Report 2025. Global Wind Energy Council, Brussels.

Haller, G., 2015. Lagrangian coherent structures. Annu. Rev. Fluid. Mech. https://doi.org/10.1146/annurev-fluid-010313-141322.

Harrison, C.S., Siegel, D.A., Mitarai, S., 2013. Filamentation and eddy-eddy interactions in marine larval accumulation and transport. Mar. Ecol. Prog. Ser. 472, 27–44. https://doi.org/10.3354/meps10061.

Jacox, M.G., Edwards, C.A., Hazen, E.L., Bograd, S.J., 2018. Coastal upwelling revisited: Ekman, Bakun, and improved upwelling indices for the U.S. West Coast. J. Geophys. Res. Oceans 123 (10). https://doi.org/10.1029/2018JC014187.

Kessouri, F., Bianchi, D., Renault, L., McWilliams, J.C., Frenzel, H., Deutsch, C.A., 2020. Submesoscale Currents Modulate the Seasonal Cycle of Nutrients and Productivity in the California Current System. Glob. Biogeochem. Cycles 34. https://doi.org/10.1029/2020GB006578.

Kim, S.Y., Terrill, E.J., Cornuelle, B.D., Jones, B., Washburn, L., Moline, M.A., Paduan, J. D., Garfield, N., Largier, J.L., Crawford, G., Kosro, P.M., 2011. Mapping the U.S. West Coast surface circulation: A multiyear analysis of high-frequency radar observations. J. Geophys. Res. Oceans 116. https://doi.org/10.1029/2010JC006669.

Lekien, F., Coulliette, C., Mariano, A.J., Ryan, E.H., Shay, L.K., Haller, G., Marsden, J., 2005. Pollution release tied to invariant manifolds: A case study for the coast of Florida. Phys. D. 210, 1–20. https://doi.org/10.1016/j.physd.2005.06.023.

Nidzieko, N.J., Largier, J.L., 2013. Inner shelf intrusions of offshore water in an upwelling system affect coastal connectivity. Geophys. Res. Lett. 40, 5423–5428. https://doi.org/10.1002/2013GL056756.

Olascoaga, M.J., Haller, G., 2012. Forecasting sudden changes in environmental pollution patterns. Proc. Natl. Acad. Sci. USA 109, 4738–4743. https://doi.org/10.1073/pnas.1118574109.

Onu, K., Huhn, F., Haller, G., 2015. LCS Tool: A computational platform for Lagrangian coherent structures. J. Comput. Sci. 7, 26–36. https://doi.org/10.1016/j.jocs.2014.12.002.

Paduan, J.D., Washburn, L., 2013. High-frequency radar observations of ocean surface currents. Ann. Rev. Mar. Sci. 5, 115–136. https://doi.org/10.1146/annurev-marine-121211-172315.

Pauly, D., Christensen, V., 1995. Primary production required to sustain global fisheries. Nature 374, 255–257. https://doi.org/10.1038/374255a0.

Payandeh, A.R., Washburn, L., Emery, B., Ohlmann, J.C., 2023. The Occurrence, Variability, and Potential Drivers of Submesoscale Eddies in the Southern California Bight Based on a Decade of High-Frequency Radar Observations. J. Geophys. Res. Oceans 128. https://doi.org/10.1029/2023JC019914.

Peacock, T., Haller, G., 2013. Lagrangian Coherent Structures: The Hidden Skeleton of Fluid Flows. Phys. Today 66 (2), 41–47. https://doi.org/10.1063/PT.3.1886.

Peng, Y., Xu, X., Shao, Q., Weng, H., Niu, H., Li, Z., Zhang, C., Li, P., Zhong, X., Yang, J., 2024. Applications of Finite-Time Lyapunov Exponent in detecting Lagrangian Coherent Structures for coastal ocean processes: a review. Front. Mar. Sci. https://doi.org/10.3389/fmars.2024.1345260.

Renner, A.H.H., 2025. Current knowledge and key gaps in understanding of offshore wind farm impacts on the physical marine environment. ICES J. Mar. Sci. https://doi.org/10.1093/icesjms/fsaf235.

Roarty, H., Cook, T., Hazard, L., Harlan, J., Cosoli, S., Wyatt, L., Fanjul, E.A., Terrill, E., Otero, M., Largier, J., Glenn, S., Ebuchi, N., Whitehouse, B., Bartlett, K., Mader, J., Rubio, A., Corgnati, L.P., Mantovani, C., Griffa, A., Reyes, E., Lorente, P., Flores-Vidal, X., Rogowski, P., Prukpitikul, S., Lee, S.H., Lai, J.W., Guerin, C., Sanchez, J., Hansen, B., Grilli, S., Matta, K.S., 2019. The global high frequency radar network. Front. Mar. Sci. 6. https://doi.org/10.3389/fmars.2019.00164.

Shadden, S.C., Lekien, F., Marsden, J.E., 2005. Definition and properties of Lagrangian coherent structures from finite-time Lyapunov exponents in two-dimensional aperiodic flows. Phys. D. 212 (3-4), 271–304. https://doi.org/10.1016/j.physd.2005.10.007.

Shadden, S.C., Lekien, F., Paduan, J.D., Chavez, F.P., Marsden, J.E., 2009. The correlation between surface drifters and coherent structures based on high-frequency radar data in Monterey Bay. Deep. Sea Res. 2 Top. Stud. Oceanogr. 56, 161–172. https://doi.org/10.1016/j.dsr2.2008.08.008.

Strub, P.T., Allen, J.S., Huyer, A., Smith, R.L., Beardsley, R.C., 1987. Seasonal cycles of currents, temperatures, winds, and sea level over the northeast pacific continental shelf: 35n to 48n. J. Geophys. Res. Oceans 92, 1507–1526. https://doi.org/10.1029/JC092iC02p01507.

Strub, P.T., James, C., 2000. Altimeter-derived variability of surface velocities in the California Current System: 2. Seasonal circulation and eddy statistics. Deep-Sea Res. II.

Strub, P.T., Kosro, P.M., Huyer, A., 1991. The nature of the cold filaments in the California Current system. J. Geophys. Res. Oceans 96, 14743–14768. https://doi.org/10.1029/91jc01024.

Trautman, N., Walter, R.K., 2021. Seasonal variability of upwelling and downwelling surface current patterns in a small coastal embayment. Cont. Shelf Res. 226. https://doi.org/10.1016/j.csr.2021.104490.

Veatch, J.M., Oliver, M.J., Fredj, E., Statscewich, H., Bernard, K., Hann, A.M., Voirol, G., Fuchs, H.L., Fraser, W.R., Kohut, J.T., 2025a. Lagrangian coherent structures influence the spatial structure of marine food webs. Commun. Earth Environ. 6. https://doi.org/10.1038/s43247-025-02101-x.

Veatch, J.M., Roarty, H., Oliver, M.J., Fredj, E., Kohut, J.T., 2025b. Attractive Lagrangian Features in the Mid-Atlantic Bight: Using Lagrangian Coherent Structures to Describe Seasonal and Interannual Changes in Circulation. J. Geophys. Res. Oceans 130. https://doi.org/10.1029/2025JC022447.

Walter, R.K., Armenta, K.J., Shearer, B., Robbins, I., Steinbeck, J., 2018. Coastal upwelling seasonality and variability of temperature and chlorophyll in a small coastal embayment. Cont. Shelf Res. 154, 9–18. https://doi.org/10.1016/j.csr.2018.01.002.

Wang, Y.H., Ruttenberg, B.I., Walter, R.K., Pendleton, F., Samhouri, J.F., Liu, O.R., White, C., 2024. High resolution assessment of commercial fisheries activity along the US West Coast using Vessel Monitoring System data with a case study using California groundfish fisheries. PLoS. One 19. https://doi.org/10.1371/journal.pone.0298868.

Wang, Y.H., Walter, R.K., White, C., Kehrli, M.D., Hamilton, S.F., Soper, P.H., Ruttenberg, B.I., 2019. Spatial and temporal variation of offshore wind power and its value along the central california coast. Environ. Res. Commun. https://doi.org/10.1088/2515-7620/ab4ee1.

Wang, Y.H., Walter, R.K., White, C., Ruttenberg, B.I., 2022. Spatial and Temporal Characteristics of California Commercial Fisheries from 2005 to 2019 and Potential Overlap with Offshore Wind Energy Development. Mar. Coast. Fish. 14. https://doi.org/10.1002/mcf2.10215.

Watson, J.R., Fuller, E.C., Castruccio, F.S., Samhouri, J.F., 2018. Fishermen follow fine-scale physical ocean features for finance. Front. Mar. Sci. 5. https://doi.org/10.3389/fmars.2018.00046.

White, C., Wang, Y.H., Walter, R.K., Ruttenberg, B.I., Han, D., Newman, E., Deyle, E.R., Gopal, S., Kaufman, L., 2024. Spatial planning offshore wind energy farms in California for mediating fisheries and wildlife conservation impacts. Environ. Dev. 51. https://doi.org/10.1016/j.envdev.2024.101005.